Predicting fretting-fatigue endurance of rotating bending shrink-fitted assemblies using a sequential RUIZ-SWT approach: The effect of entrapped debris layer

B. Dieu, Siegfried Fouvry, V. Doquet, F. Bridier

B. Dieu, S. Fouvry, V. Doquet, F. Bridier, Predicting fretting-fatigue endurance of rotating bending shrink-fitted assemblies using a sequential RUIZ-SWT approach: The effect of entrapped debris layer, Tribology International 186 (2023) 108593 (https://doi.org/10.1016/j.triboint.2023.108593)

Predicting the fretting-fatigue endurance of rotating bending shrink-fitted assemblies using a coupled RUIZ-SWT approach: the effect of entrapped debris layer

B. Dieu [(a,b)], S. Fouvry [(a)*], V. Doquet [(b)], F. Bridier [(c)]

(a): Laboratoire de Tribologie et de Dynamique des Systèmes, École Centrale de Lyon, Ecully, France

(b): Laboratoire de Mécanique des Solides, CNRS, École Polytechnique, Palaiseau, France

(c): Naval Group - Technocampus Ocean, Bouguenais, France

*corresponding authors: S. Fouvry (siegfried.fouvry@ec-lyon.fr); B. Dieu (benjamin.dieu@ec-lyon.fr); V. Doquet (veronique.doquet@polytechnique.edu); F. Bridier (florent.bridier@naval-group.com)

Abstract: Fretting-fatigue damage often appears in shrink-fitted assemblies submitted to rotating bending. This paper focuses on the influence of the sleeve edge geometry on such damage. Rotating bending test have been performed with shrink-fitted assemblies. Observations of broken and unbroken specimens confirmed the fretting-fatigue phenomenon, and provided a better understanding of the crack nucleation process. A 3D finite element method model was developed to evaluate the sliding and opening lengths A sequential tribological - fatigue stress analysis strategy allowed the prediction of the maximum crack location ($X_{\Gamma max}$ Ruiz criterion) then the estimation of the fatigue endurance of the assembly using the SWT criterion. The last step of this $\sigma_{SWT}(X_{\Gamma max})$ approach considers the presence of a debris layer within the contact to improve the consistency of the service life prediction.

Keyword: Fretting Fatigue, shrink fitted assemblies, SWT fatigue criterion, Ruiz criterion

Nomenclature

a (µm)	Crack length
C10	Name of the specimen geometry showing a 10 mm fillet
d (mm)	Distance between to the contact border, along the shaft axis
F (N or kN)	Bending force
h (µm)	Debris additional thickness entrapped within the interface
h_W *(µm)*	Worn thickness (Third Body theory)
h_{exp} *(µm)*	Measured additional thickness of the debris layer
h_{num} *(µm)*	Maximal additional thickness of the debris layer in the simulation
h_{tb} *(µm)*	Third body thickness (Third Body theory)
$h_{tb,ss}$ *(µm)*	Steady state third body thickness (Third Body theory)
L_I *(mm)*	Length of zone I
L_{II} *(mm)*	Length of zone II
L_{III} *(mm)*	Length of zone III
Nc	Loading cycles at failure (Δu = 10%)
p_{nom} *(MPa)*	Nominal contact pressure
R3	Name of the configuration geometry showing a 3 mm radius round
u (mm)	Deflection of the specimen (measured at mid-length)
$X_{\Gamma max}$*(mm)*	Position (i.e. distance from the contact border) where Γ_{SWT} is maximum
α	Angle between the crack and the normal to the contact surface
λ_{ref} *(µm)*	Diametric interference
δ_s*(µm)*	Sliding distance during a loading cycle
ϵ_a	Strain amplitude imposed to the critical plane $\vec{n}$
λ_{ref} *(µm)*	Diametric interference
σ_1*(MPa)*	Principal stress
$\sigma_{n,max}$*(MPa)*	Maximum normal stress imposed to the critical plane $\vec{n}$
$\sigma_{d,-1}$*(MPa)*	Alternated traction - compression fatigue limit
$\sigma_{SWT}(MPa)$	Smith-Watson-Topper equivalent stress
$\sigma_{SWT}(X_{\Gamma max})(MPa)$	SWT stress at the $X_{\Gamma max}$ position
$\tau_x(MPa)$	Surface shear stress
τ_d *(MPa)*	Torsion fatigue limit
Γ (MPa²×mm)	Ruiz Parameter
$\Gamma_{\mathrm{SWT}}(MPa)$	Smith-Watson-Topper parameter
ϕ (µm^3/cycle)	Debris flow (Third Body theory)

1 INTRODUCTION

Fretting is a contact damage which occurs when two surfaces are kept in contact while having a relative oscillatory motion [1]. It may lead to wear, crack nucleation and propagation. Combined with bulk fatigue, it may lead to early breakage of the damaged part. The so called fretting-fatigue damage can lead to a sharp reduction of the assemblies lifespan [2]–[4].

Interference fitting is usually used to fasten two axisymmetric tight-mating parts. This kind of assembly may be subjected to fretting-fatigue, as it has been reported in rail transportation [5]–[8], wind turbines [9] and naval transmission axles [10], [11].

This paper focuses on the latter case. Shrink- fitted assemblies are commonly used in fluid bearings to ensure dry environment within the component. These shafts are subjected to bending due to the weight of components. The bending of such assemblies leads to small slips between the axle and the sleeve. Since the shaft rotates, a rotating bending load is applied and may lead to fretting-fatigue damage.

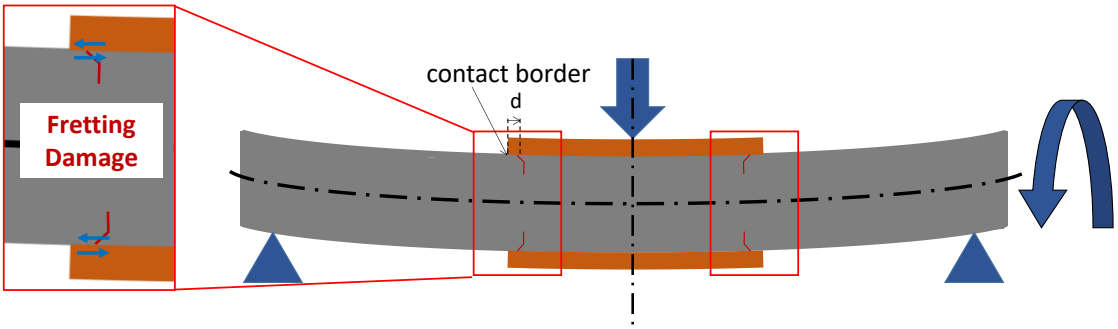

Fig. 1: Fretting-fatigue between sleeve and transmission shafts.

Slip occurs at the borders of the contact, near the edges of the sleeve (**Fig. 1**). At this precise location in the shaft, fretting-fatigue can initiate cracks, which can propagate, due to fatigue loading.

The main objective of this paper is to predict the failure risk on shrink-fitted assemblies under rotating bending. The studied case will feature a bronze sleeve and a steel shaft. Moreover, the nominal contact pressure studied here, below 30 MPa, is significantly lower than most other cited applications [3], [5], [7], [8], [10], [11], generally ranging from 70 MPa to 247 MPa. Beside, since the sleeve edge geometry highly influences the contact pressure profile and therefore the fretting stressings, there is a crucial interest to optimize this latter in order reduced the fretting fatigue cracking risk [2], [3], [5]–[8]. Moreover due to the relative sliding at the contact edges surface wear damages are occurring modifying the local contact geometry, the stress filed and finally the fretting fatigue cracking process [12].

These various aspects will be investigated developing an original experimental-numerical strategy including the following steps:

- Design of a representative test bench, including specimen manufacturing and shrink fitting

- Study of the influence of the sleeve edge geometry regarding the endurance in fretting-fatigue
- Analysis of damage
- Introduction of a simple modelling strategy based on a sequential tribological-fatigue analysis to predict first the crack nucleation location and then the fatigue endurance. This approach will consider the third body layer generated between the sleeve and axle, which was shown to dramatically influence the distribution of contact stresses.

2 EXPERIMENTAL PROCEDURE

2.1 Materials

Steel shaft

The axles are made of 16MND5 bainitic steel Table 1), with former austenic grains of approximately 35 µm (Fig. 2). An analysis of the very same material has been published by Petureau *et al.* [13]. Its composition is detailed in Table 1. The Young's modulus is E_{steel} = 210 GPa, and the ultimate tensile strength R_m = 652 MPa. A Poisson's coefficient v_{steel} = 0.3 was considered. Fatigue tests under fully reversed loadings yielded the endurance limits in torsion: τ_d , and in tension: $\sigma_{d,-1}$ (not provided for confidentiality reasons).

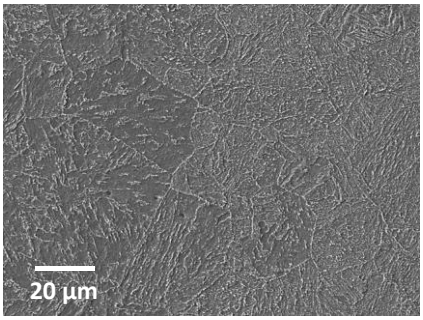

Fig. 2: Microstructure of the bainitic steel, SEM, SE, after polishing and a 10s Nital etching.

Table 1: Chemical composition of the 16MND5 steel in mass percent.

C	Si	Mn	P
≤0.2	≤0.4	1.15 to 1.55	≤0.025
S	**Ni**	**Mo**	**Fe**
≤0.01	0.5 à 0.8	0.45 to 0.55	balance

Bronze sleeve

The sleeves are made of CuSn12 bronze, whose composition is detailed in Table 2. The elastic properties considered are: E_{bronze} = 110 GPa and v_{bronze} = 0,3.

Table 2: Chemical composition of the CuSn12 bronze in mass percent.

Ni	Pb	Sn	Zn	Sb	P
≤2	≤2.5	10 to 13	≤2	≤0.15	≤0.6
Al	**Fe**	**Mn**	**S**	**Si**	**Cu**
≤0.01	≤0.2	≤0.2	≤0.05	≤0.01	83 to 87

2.2 Design and manufacturing of the shrink-fitted rotating specimens

Specimens consist in shrink fit assemblies of steel shafts and bronze sleeves, as displayed in Fig. 3. The external diameter of bronze sleeves, $D_{ext,sleeve}$, is 55 mm, while the internal diameter, $D_{int,sleeve,}$ is 45 mm. The whole inner surface of the sleeves is grinded to reach the specified internal diameter. The steel shafts are solid axles with an external diameter D_{shaft} close to 45 mm and a total length L_{shaft} of 550 mm. They are turned and grinded to the proper diameter, in order to be paired with the sleeves, while ensuring the right interference. Both the axle and sleeve grinded surfaces display a roughness R_a of 0.2 µm.

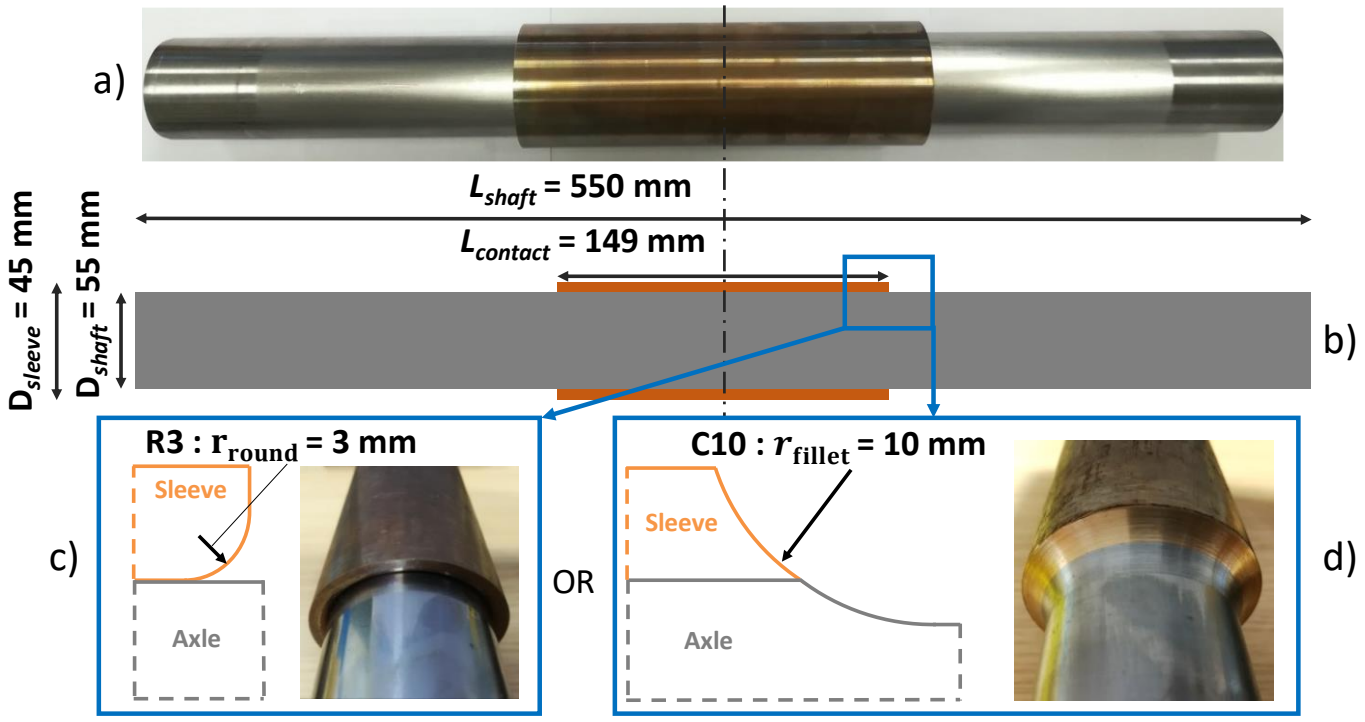

Fig. 3: Picture of the specimen a) and its design b), with c) the R3 and d) the C10 sleeve geometries.

The two parts are then shrink- fitted using a dedicated apparatus (Fig. 4). The bronze sleeve is heated by heating collars up to 300 °C, and the shaft is then inserted vertically at the right position, using a hydraulic actuator. The process is sufficiently fast not to induce contact between the two mating surfaces during the movement. The correct insertion of the shaft is ensured by a precise positioning of the sleeve, and live measurement of the actuator displacement sensor. Once the shaft positioned, the sleeve is cooled down by ambient air.

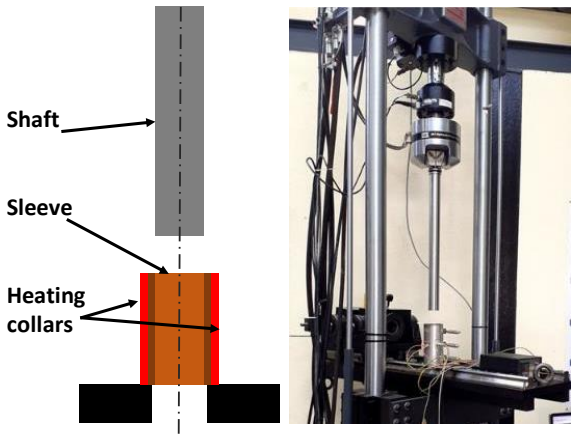

Fig. 4: Shrink fitting apparatus, hydraulic actuator and heating collars.

As mentioned previously, the influence of the geometry of sleeve edges is of prime importance [14], and will thus be emphasized. Two configurations have been used (Fig. 3). For the first one, denoted as R3, the sleeve shows a 3 mm round at both inner ends, and the shaft is smooth. The second one, denoted as C10, is obtained through a careful machining of an R3 specimen after shrink fitting process (Fig. 3d). Cross section observations confirmed that the post C10 machining process do not affect the shaft microstructure and the related mechanical properties. Moreover, the domain of interest where fretting cracking is occurring (i.e. below the fretted interface), remains far away from the post C10 machined surface. Special cautions were applied to ensure that the contact length $L_{contact}$ remains the same for both R3 and C10 geometries (149 mm). The diametric interference λ_{ref} is defined as the difference between the external diameter of the shaft D_{shaft} and the internal diameter of the sleeve $D_{int,sleeve}$. The diametric interference λ_{ref} (not provided for confidentiality reasons) was chosen to ensure the desired nominal pressure p_{nom} (*i.e.* pressure at the centre of the contact after fitting), estimated using an infinite shaft and sleeve hypothesis [15]. The exact value of p_{nom} cannot be provided for confidentiality reasons but was estimated below 30 MPa.

2.3 Rotating bending test bench

A three points rotating bending bench has been developed (Fig. 5). A motor rotates the specimens under a constant bending load at a frequency f =15 Hz. Two rolling bearings are situated near the ends of the shaft. A system of screws and springs moves the central rolling bearing downwards, and thus bends the whole specimen. Hence the bending force F is applied manually, but continuously monitored, using a force sensor. Moreover, a displacement sensor measures the induced deflexion u of the specimen at mid-length. The rolling parts are water-cooled. A LabVIEW® system is implemented to record the bending force F, the bending displacement, u, and the angular position θ (200 points per cycle). The number of rotations at failure N_c is used to quantify the fatigue life.

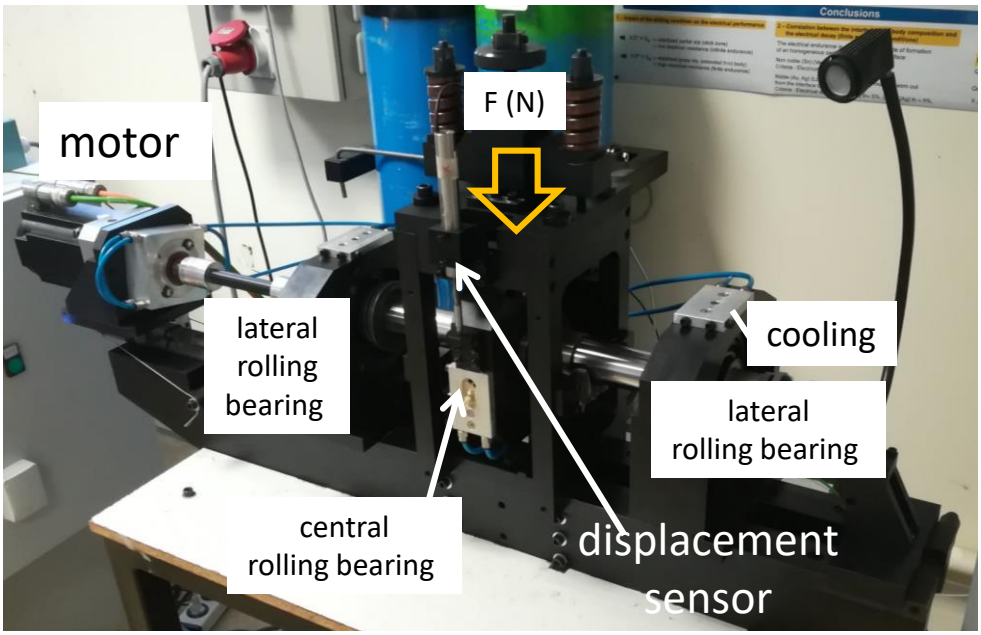

a)

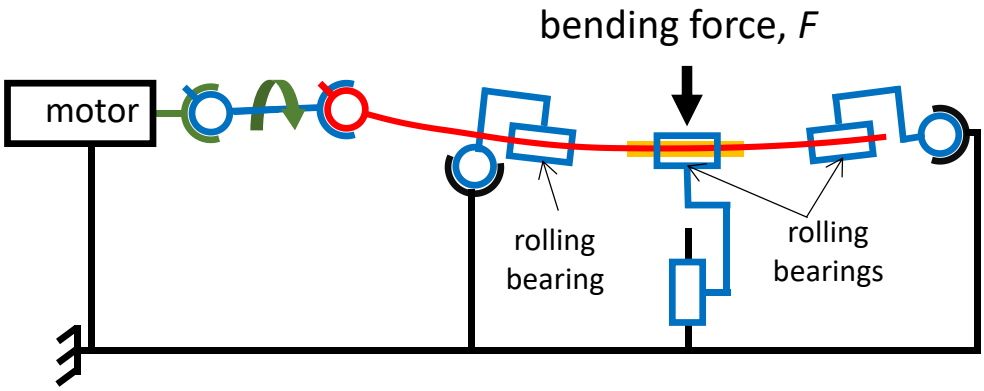

b)

Fig. 5: Rotating bending bench (sleeve-axle shrink-fitted specimen is rotating through 2 laterals rolling bearing in contact with the axle surface and a central rolling bearing in contact with the external part of the bronze sleeve): a) global overview; b) schematic of the kinematics of the test bench.

A full failure of the specimen tends to deteriorate the fracture surface and the contact surface, limiting the damage expertise. Therefore, the tests were stopped whenever the bending deflexion increases by 10 % above the initial value. This corresponds to a crack extension longer than 20 mm, close to the shaft failure condition. The run-out value was fixed at 2.10^7 cycles.

3 FEM MODELLING

To better quantify the contacts loadings and successively predict the cracking a 3D finite element model has been developed using Abaqus (v6.14.2) to simulate each experiment. This model simulates the bending of the sleeve and shaft assembly. A bronze sleeve is fitted on a solid steel

shaft Fig. 6. The materials are considered isotropic and elastic. Their mechanical properties were mentioned in section 2.1. The first geometries are considered perfect, and do not consider wear. A cross plane symmetry at the centre of the specimen allows a reduction of the size of the model. X is the axial direction and Z is the bending force direction. Translation along X axis are hence blocked at the symmetry plane.

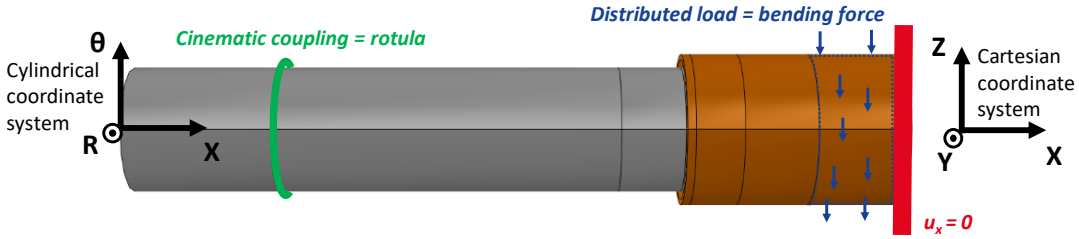

(a)

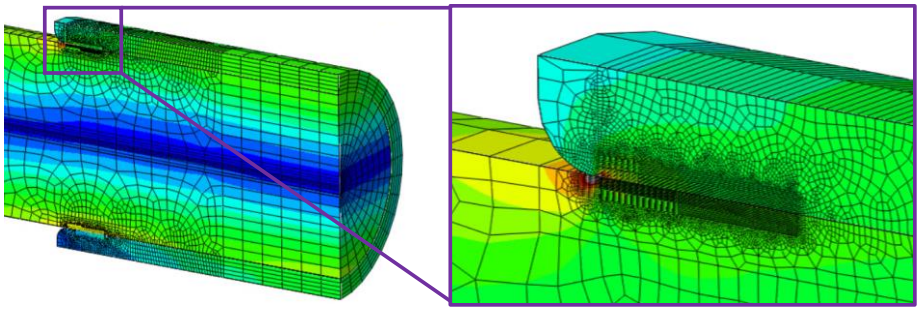

(b)

Fig. 6: (a) 3D finite element model using a cross plane symmetry, with the two parts assembled; (b) detailed of the mesh strategy of the FEA model.

Regarding the mesh, 8-node linear brick elements with reduced integration and hourglass control (C3D8R on Abaqus) have been used. The mesh displays a 10° periodicity around the shaft axis, and was refined near the interest zones (*i.e.* contact borders) to obtain 50x50 µm element in the *r*-x plane. The high aspect ratio, reaching 80 in the worst case (*i.e.* the refined zone for criteria computation), does not influence significantly the stress computations. Indeed, a refined model involving elements with aspect ratios of 40 and 20 in the worst cases was compared with the actual model for the lowest loading condition. A difference of less than 0.1% on the axial stress was found. This confirms the relevance of the given simplified model whose computation time (shorter than 4 hours) allows a systematic analysis of all the experiments which was not possible to address using the refined model.

The outer bearings are modelled as ball joints, with translation along x as an additional free degree of freedom. The central bending force is applied through a so-called surface traction on a 32 mm band on the outer skin of the sleeve.

The first step of the computation (Fig. 7) consists in a fitting stage, using a repulsion sequence as described by Lorenzo et al. [16]. It consists in the contact interaction being activated after the shaft is fully pushed within the sleeve. It is followed by two complete reverse bending cycles. We assume that the data extracted from the X-Z plane under alternating bending is equivalent to the data for the same plane under rotating bending. The last cycle (between computation step 2 and 3, Fig. 7) is then considered for the stress and strain post processing analysis including the slip and contact opening investigations (section 4) and the cracking simulations (section 5).

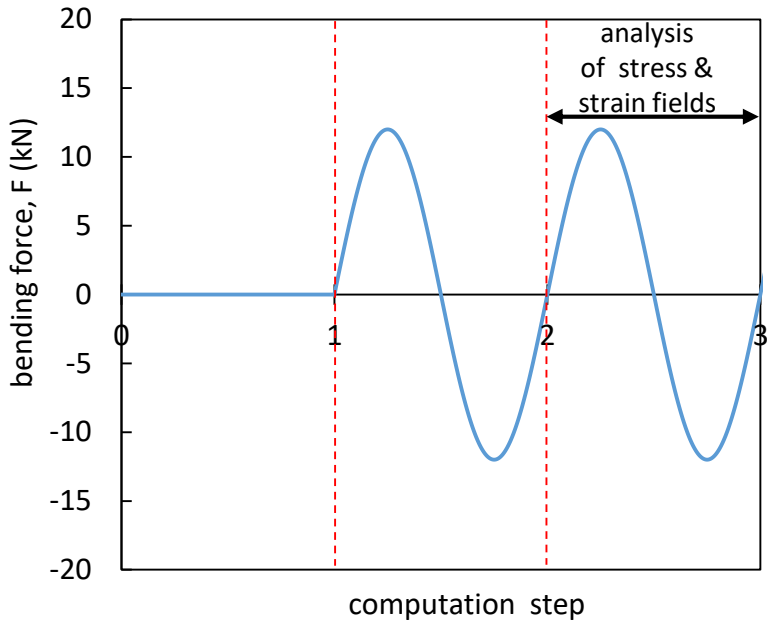

Fig. 7: Time evolution of the bending force along calculation steps.

The contact is modelled with a friction coefficient of 0.8. This friction value was previously determined performing plane (16MND5) on plane (CuSn12) fretting tests using the methodology detailed in [17]. A penalty formulation was used to enforce contact conditions in both normal and tangential directions. The comparison with an augmented lagrangian formulation in a simplified loading case is used to determine the appropriate value of the Abaqus parameter named elastic slip. A value of 0.1 µm ensures precise results and avoid convergence issues. Hence, an interface is considered sliding when the calculated sliding amplitude exceeds 0.1 µm. Contact geometrical smoothing has been applied to better capture the interaction between the two curved surfaces. The shaft bears the slave surface.

4 EXPERIMENTAL RESULTS

4.1 Comparison of the fatigue endurances

The test results are compiled in Table 3, and displayed in Fig. 8. The lives of C10 specimens were at least 3 times longer than those of their R3 counterparts under the same loading. The sleeve edge geometry thus has a strong influence on the sensitivity of the assembly to fretting-fatigue.

Table 3: Test results.

Sleeve edge geometry	Bending force, *F* (N)	$\sigma_{xx}/\sigma_{d,-1}$	N_c
R3	18,000	0.48	$1.78\ 10^6$
R3	15,000	0.40	$2.83\ 10^6$
R3	13,500	0.36	$1.35\ 10^7$
R3	12,750	0.34	$6.76\ 10^6$
R3	12,000	0.32	$>2{,}00\ 10^7$
R3	10,500	0.28	$>2.00\ 10^7$
C10	18,000	0.48	$4.30\ 10^6$
C10	18,000	0.48	$5.33\ 10^6$
C10	16,500	0.44	$1.25\ 10^7$
C10	15 ,750	0.42	$1.87\ 10^7$
C10	15 ,000	0.40	$>2.00\ 10^7$
C10	13 ,500	0.36	$>2.00\ 10^7$

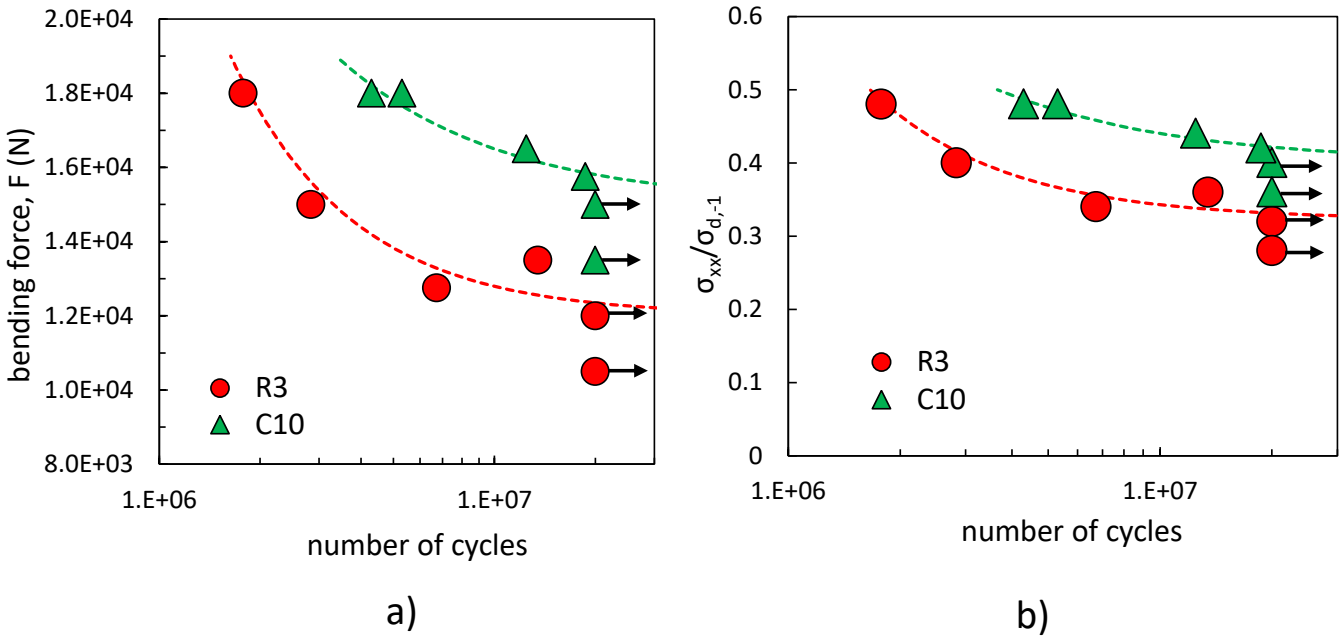

Fig. 8: Rotating bending tests results: evolution of assemblies fatigue lives a) with the bending force, b) with the estimated axial stress range at the contact border divided by $\sigma_{d,-1}$.

A one dimensional model has been developed to allow a fast comparison of the local stress ranges σ_{xx} between the two configurations, for a given bending load. It is based on Euler-Bernoulli's beam theory, and does not consider the contact, but features a unique part, whose sectional mechanical properties are derived from those of the steel shaft and the bronze sleeve.

The stress ranges displayed on Fig. 8b are those of the axial stress σ_{xx} calculated at the contact border (*i.e.* considering the shaft section). The figure shows that the endurance limit at 2.10^7 cycles for C10 specimens is approximately 20 % higher than for R3.

Overall, as compared to conventional uniaxial fatigue, fretting-fatigue reduces the endurance limit of the material, by almost 66 %. This endurance reduction is consistent with former results obtained for similar test configurations, by Shu *et al.* [18] (reduction of 54%) or Lee *et al.* [19] (reduction of 50%).

4.2 Damage analysis

Facture surface of a fully broken specimen

The R3 specimen submitted to F = 15 kN is used to illustrate the typical damage observed following the rotating bending experiments. It fractured at $N_c = 2.83.10^6$ cycles (Fig. 9), bypassing the Δu = 10 % stop condition. The main crack was situated under the contact, d= 3 to 4 mm from the contact border, along the axial direction (i.e. d the distance from contact border toward the inner part of the sleeve-axle contact). The fracture surface analysis Fig. 9 shows several cracks nucleation sites, all over the perimeter of the shaft as also observed by Song *et al.* [5] as well as Leidich *et al.* [8]. The initiation sites are located in various transverse sections, each small crack then coalescing with surrounding cracks to form a bigger one. This indicates that crack nucleation is caused by contact stresses distributed over a large zone.

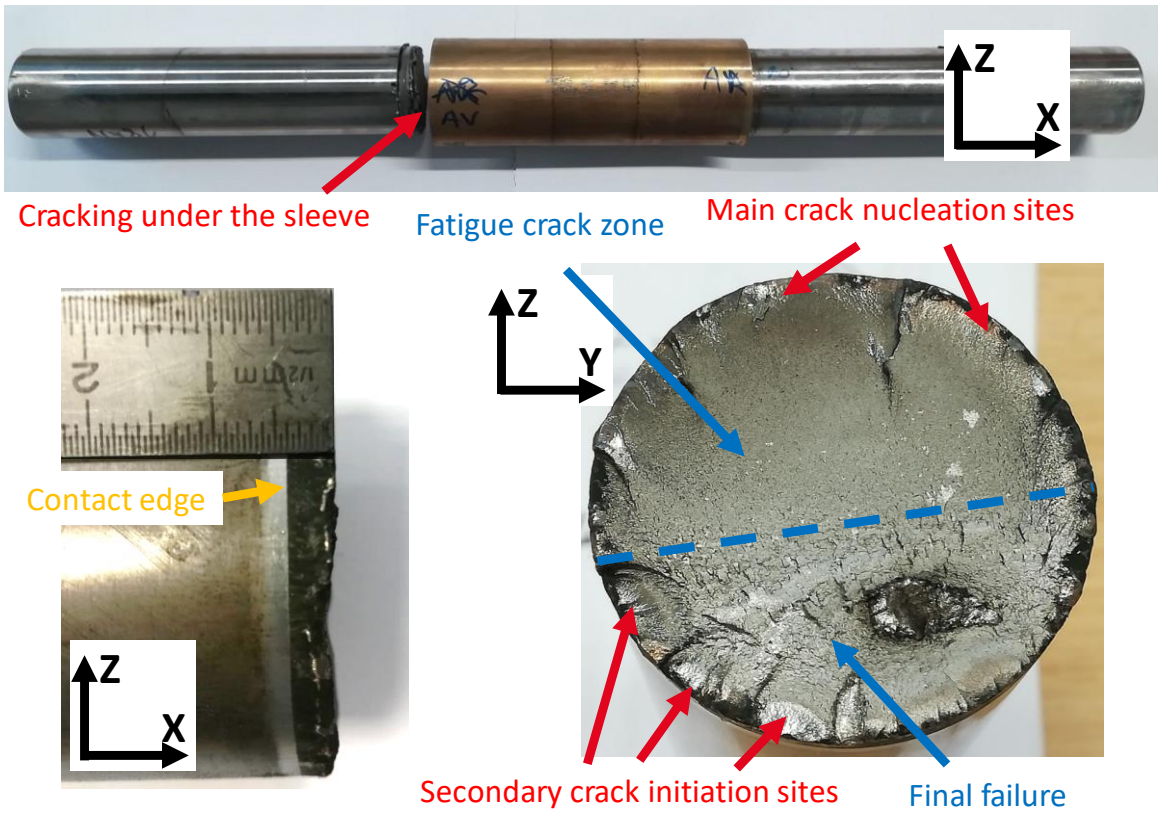

Fig. 9: Observation of a fully broken R3 specimen.

Contact surface damage

The C10, submitted to F = 15 kN, (run out at 2.10^7 cycles) was investigated to determine the main characteristics of contact surface damage. The sleeve was cut open and removed. Three zones were identified on the contact surface (Fig. 10a). The central stick zone (zone I) where no slip occurs between the two part along the whole test has a bright aspect. Its length is denoted by L_I. Zone II appears on both sides, and displays dark oxides, mainly magnetite (Fe_3O_4) as suggested by the colour [20] and as confirmed by Raman spectrographic analysis (Fig. 10b). Within this zone some slip occured between the two parts, but with a low oxygenation level. By contrast, the oxides observed in zone III display a higher level of oxygenation. Raman spectroscopy indicates that it is mainly constituted of hematite (Fe_2O_3) appearing brown [20]. Debris and surface oxidation is due to the partial opening of the sleeve under bending, as described by Radi *et al.* [21]. Because the lengths of zones II and III vary along the circumference of the shaft, the mean size of the zone will be used below, and denoted by L_{II} and L_{III}.

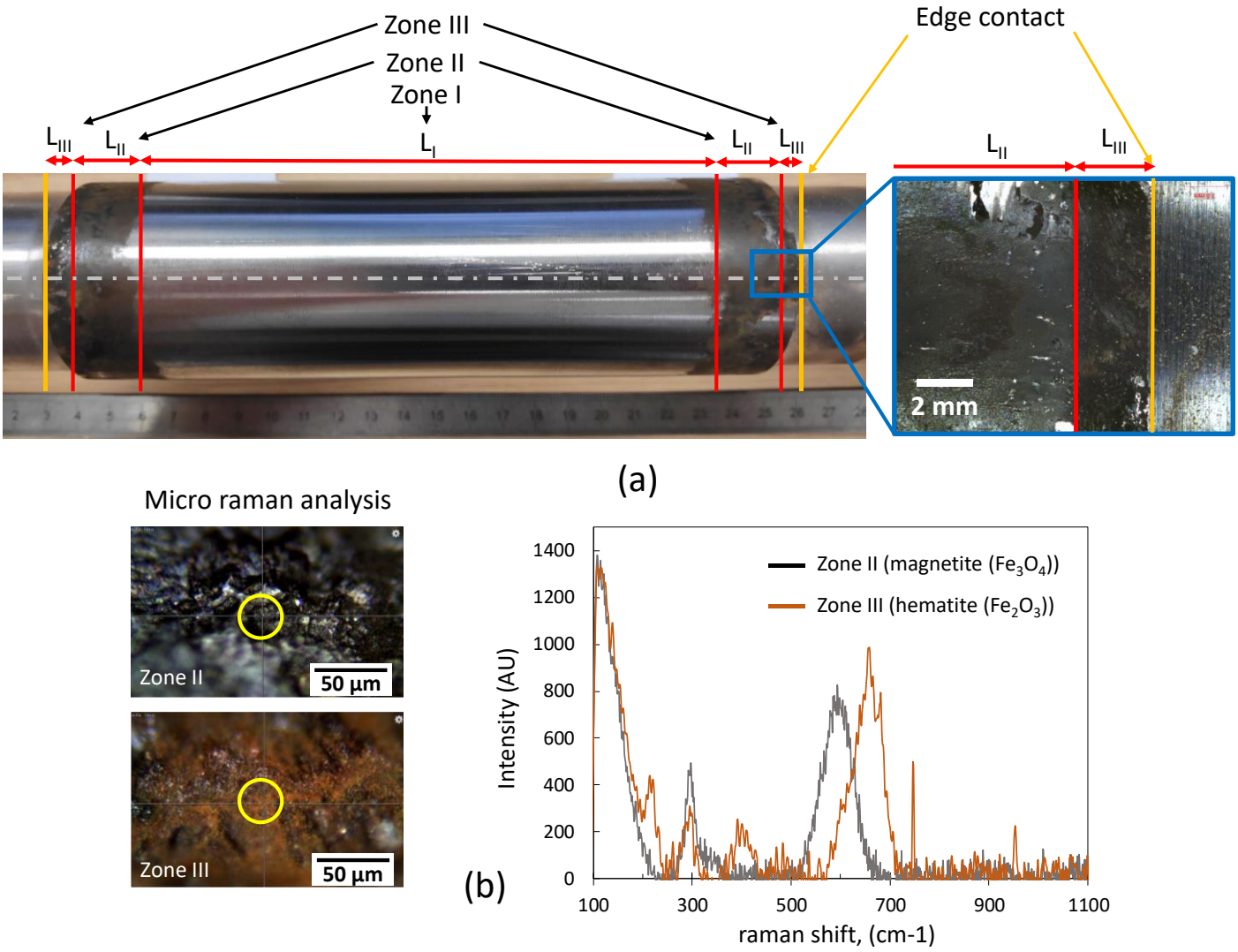

Fig. 10: a) Surface damage for C10, 15 kN, 20E6 cycles; b) Raman analysis in Zone II and III (Horiba XploRA, laser 633 nm).

The mean lengths of zones II and III in all the specimens have been compiled in the following graphics (Fig. 11). The solid bars represent experimental data, whereas the dotted ones are the numerical predictions given by the 3D FEM computation. For all configurations the sliding zone length (II + III), increases with the bending load. It is interesting to note that contact opening is occasionally observed for R3 contact configuration but systematically observed for C10 contact geometry. These experimental observations are consistent with the simulations which predict contact opening only for C10 contact geometry. This can be explained by the fact that R3 configuration induces much higher contact pressures at the contact border than C10 geometry. Hence it can be explained the occurrence of zone II (i.e. low level of oxygenation=> Fe_3O_4) and zone III (i.e. higher level of oxygenation=> Fe_2O_3). Zone II corresponds to the domain where

sliding is occurring (i.e. allowing debris formation) but the interface is never directly exposed to ambient air leading to a lower level debris oxidation. By contrast, zone III involves contact sliding and contact opening allowing a direct ambient air exposure which promotes a higher level of debris oxidation. Confirming former literature works [21], both simulations and experiments suggest that the higher the bending force *F*, the longer the total slip domain $L_{slip}= L_{II} + L_{III}$. The comparison between the two sleeve geometries also indicates that for a similar bending force, the total slip domain is longer for the C10 geometry than for the R3 configuration. To conclude, a suitable correlation is observed between experiments and 3D FEM simulations which indirectly support the relevance of the given FEM model as well as the friction value (i.e. μ= 0.8) applied for the computations.

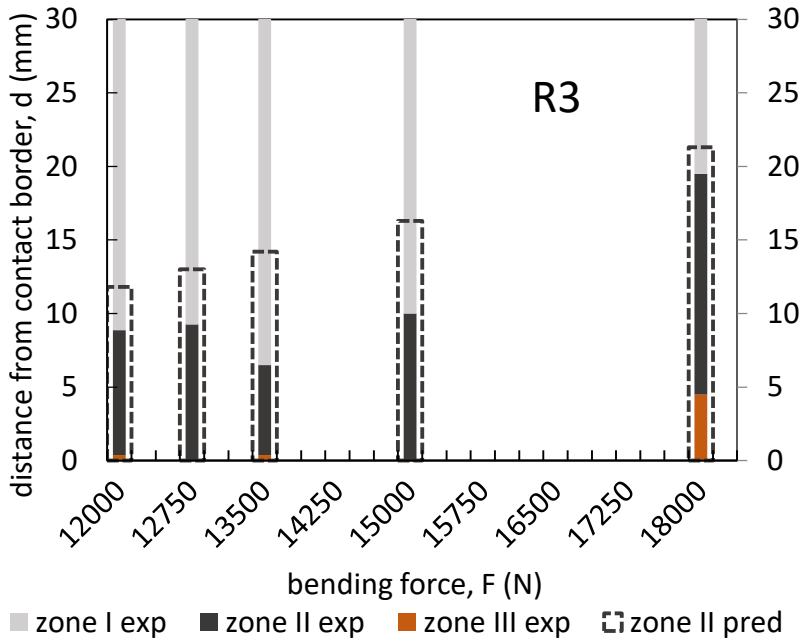

a)

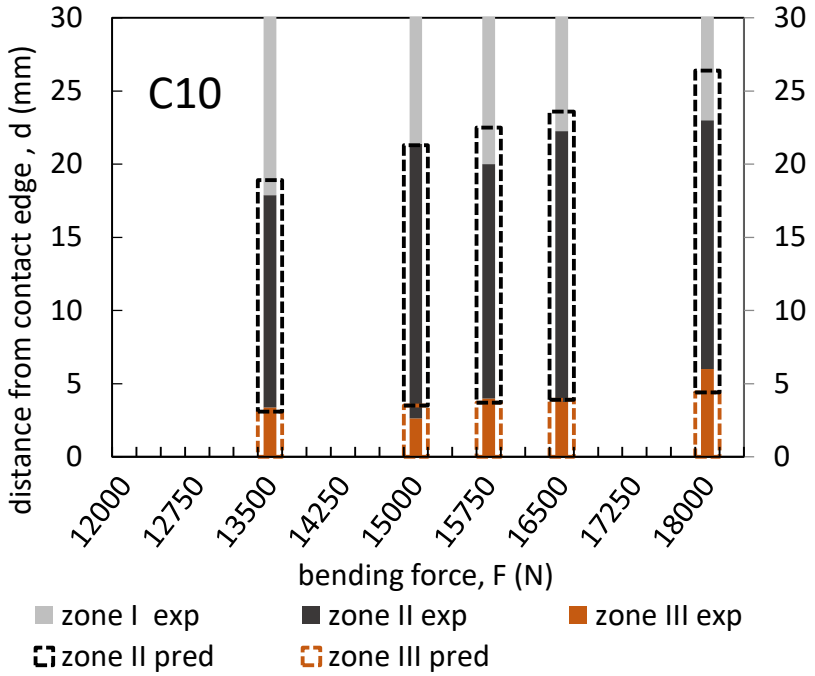

b)

Fig. 11: Analysis of sliding zone lengths: comparison between experimental measurements and numerical prediction for a) R3 specimens and b) C10 specimens.

Damage analysis on run out specimen

A protocol was developed to study the in-depth extension and location of the cracks in run out specimens. After separation of the sleeve and the shaft, a transverse section of the shaft containing the sliding zone II and III was extracted (Fig. 12) and cut in several pie-like parts. Each part was then mounted in epoxy resin and polished to a mirror-like surface. Each crack position in terms of distance from the contact border *d*, as well as its length *a* and its angle α relative to the normal to the contact surface were compiled (see Fig. 12).

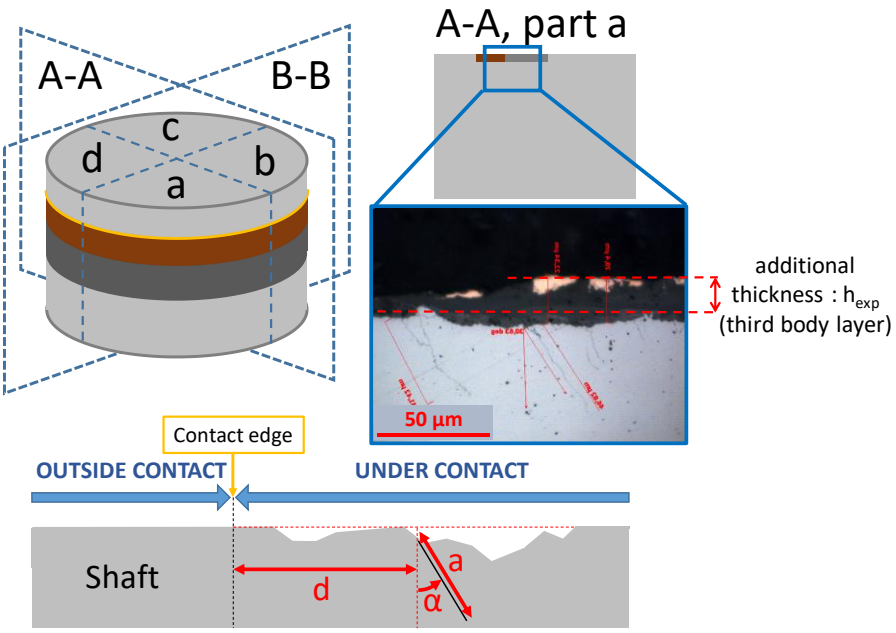

Fig. 12: Cross section expertise of specimens.

The crack expertise focused on the two run out specimens with the highest loads, *i.e.*, R3_12kN and C10_15kN. All the crack initiated from the contact surface, and 80 % propagated towards the inner side of the contact, which is characteristic of fretting-induced cracking. Roughly, they display a 45° α angle versus the normal to the surface, in accordance with the observations made by Song *et al.* [5] and Zhang *et al.* [10].

Specimen R3_12kN exhibits nearly no zone III (L_{III} < 0.5 mm). It means that bending and wear were insufficient to allow an access of ambient air to the fretted interface. In this sample, all cracks were located inside zone II (see Fig. 13), with deeper cracks around *d* = 1mm, close to the contact border. Although some of the cracks on Fig. 13a seem to be outside the average width of zone II, they are in fact inside zone II, whose local extension varies along the perimeter of the specimen.

By contrast, specimen C10_15kN displays a zone III (Fig. 13b), in which no cracks were initiated. Like in the previous specimen, all cracks initiated within zone II, with the deepest crack located next to the outer border of the zone.

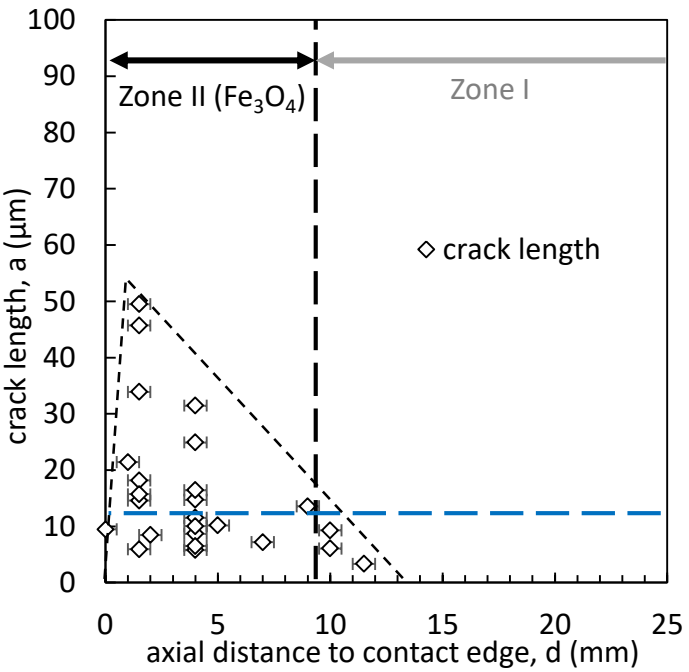

(a)

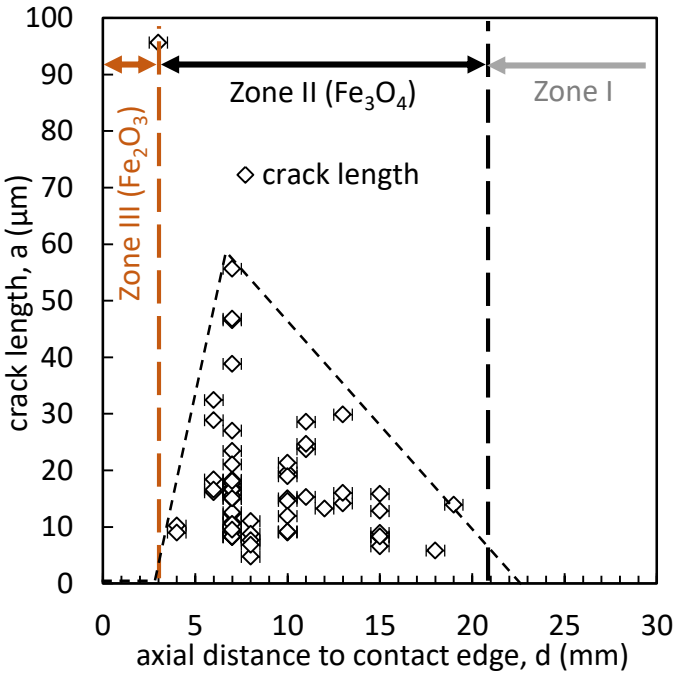

(b)

Fig. 13: Cracks length “a” measured from the reference surface of the axle (see Fig. 12) as function the axial distance from the contact border “d” (a) R3_12 KN and C10_15 KN.

Debris generated by friction between the two parts tend to stick to the axle surface. Due to the contact configuration they are not ejected from the interface, and therefore they accumulated

during the test. The powder structure and the oxidation process increase the specific volume compared to the original materials. Hence the accumulation of this debris layer induced an additional thickness within the interface, which potentially can modify the contact pressure distribution, and finally the stresses. The estimation of the debris layer profile using conventional surface profilometer for such contact configuration is particularly complex due the difficulty in assessing the reference line of the sleeve surface. Therefore the thickness of the debris layer was “optically” estimated from steel axle and bronze sleeves cross section observations (Fig. 12). Fig. 14 shows the debris layer thickness as a function of the distance from the contact border (h_{exp}) for the two geometries. Again some differences can be observed between R3 and C10 contact configurations. For the R3 contact the maximum debris layer thickness ($h_{exp,max}$ = 30µm) is found next to the contact border (i.e. around d= 1 mm). Then, the thickness decreases to a plateau value h_{exp} ≈ 11µm which extends from d = 4 to 12mm. Then it finally decreases to zero above d= 15 mm. The C10 contact displays a much more extended distribution of the debris layer thickness. It is negligible from d=0 to 3 mm. Then it rises to a maximum value ($h_{exp,max}$ = 25µm) around d = 7 mm, to finally decrease asymptotically to zero when d= 22mm. These third body distributions will be assumed stable, and implemented in the contact stressing analysis described below, to predict the cracking processes.

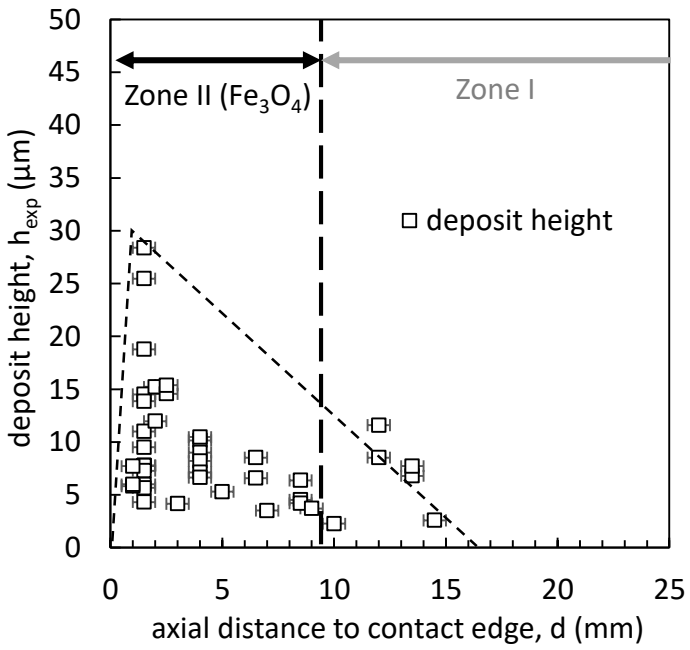

(a)

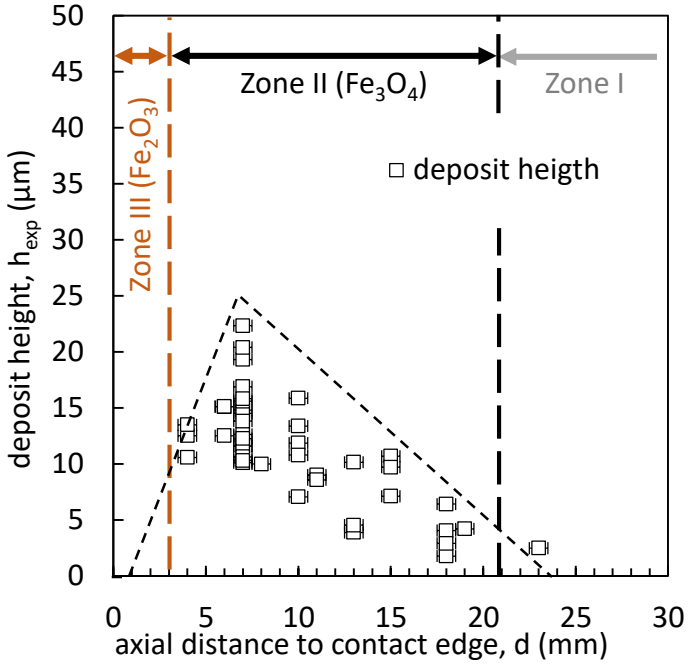

(b)

Fig. 14: Comparative study of debris layer height between specimen R3_12kN and C10_15kN (the debris layer height is estimated from optical measurements of the cross section observations).

5 FRETTING FATIGUE ENDURANCE PREDICTION

5.1 Crack nucleation modelling

To tackle the crack initiation prediction, two criteria where first considered. The first one is Smith-Watson-Topper (SWT) [22] equivalent fatigue stress parameter σ_{SWT} expressed as

$$\Gamma_{\mathrm{SWT}} = \max_{\vec{n}}\left(\sigma_{n,max} \times \epsilon_a\right) \quad (1)$$

$$\sigma_{SWT} = \sqrt{E.\Gamma_{\mathrm{SWT}}} = \sqrt{E.\sigma_{n,max}.\epsilon_a} \quad (2)$$

with $\sigma_{n,max}$ the maximum tensile stress on the plane of normal $\vec{n}$ and ϵ_a the corresponding strain amplitude. The maximum value is estimated at each integration point and computed on every possible plane of normal $\vec{n}$ (with a increment of 10°).

The second is Ruiz parameter [23] combining tribological parameter (the sliding amplitude and the surface shear on the interface) with the maximum principal tensile stress.

$$\Gamma = \left(\sigma_1 \times |\tau_x| \times \delta_s\right)_{max} \quad (3)$$

with σ_1 the first principal stress, τ_x the surface shear and δ_s the surface sliding amplitude. The Ruiz parameter Γ is computed only on the surface and cannot be considered to investigate subsurface damage. By contrast to the SWT approach which can be considered as a “pure” fatigue stress approach, the Ruiz approach appears as a “hybrid” criterion combining in a single variable both fatigue stresses and contact tribological loadings. Fig. **15** compares the experimental crack length a versus the σ_{SWT} SWT fatigue stress and the Γ Ruiz parameter. The correlation is rather poor for SWT, suggesting that it would not be able to capture the crack nucleation process of the studied interface. The Γ Ruiz parameter catches fairly well the distribution of the crack and their relative length. The Γ Ruiz parameter performs also well on the C10 geometry as shown by Fig. 16.

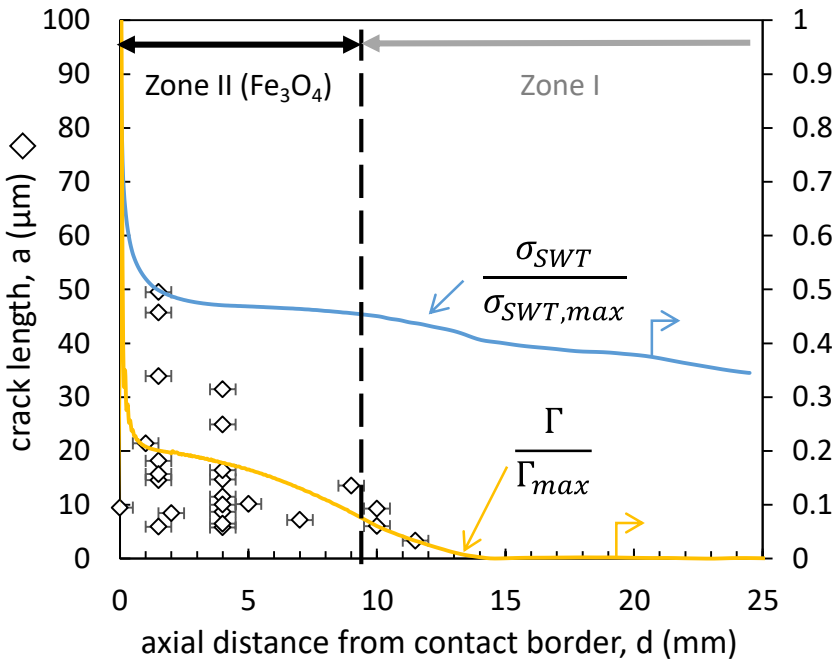

Fig. 15: Comparison between the crack length measured on the R3_12kN test and the normalized distribution of the crack nucleation criteria ($\boldsymbol{\sigma_{SWT}/\sigma_{SWT,max}}$, $\boldsymbol{\Gamma/\Gamma_{max}}$).

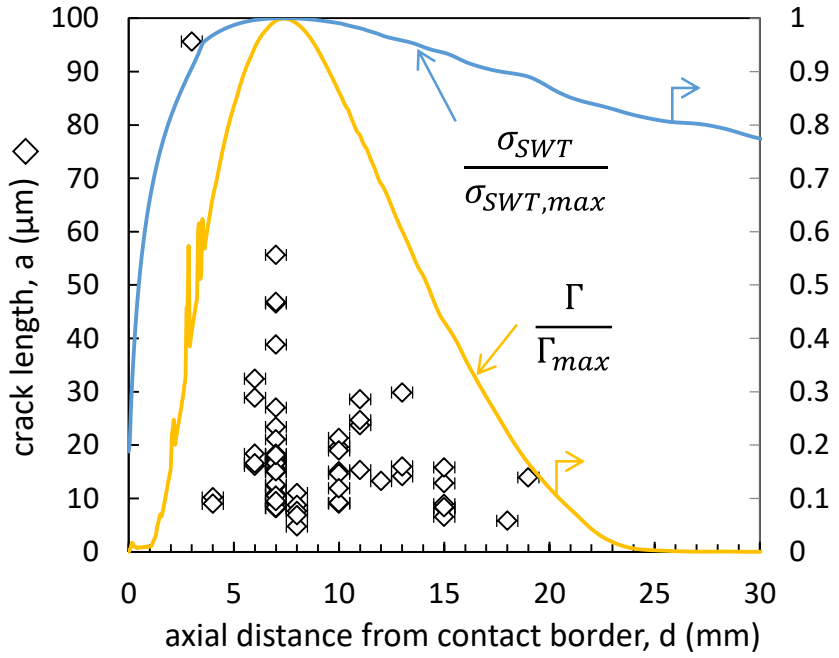

Fig. 16: Comparison between the crack length measured on the C10_15kN test and the normalized distribution of the crack nucleation criteria ($\boldsymbol{\sigma_{SWT}/\sigma_{SWT,max}}$,$\boldsymbol{\Gamma/\Gamma_{max}}$).

The expertise underlined the development and trapping of a significant debris layer localizing the surface stressing and potentially influencing the stress level and distribution, and thus crack

initiation. It was therefore assumed that surface wear and the resulting formation of a debris layer are the driving factors of the crack nucleation process: the thicker the debris layer, the higher the contact stresses, and therefore the higher the crack nucleation risk.

Due to the formulation of Γ involving both sliding amplitude and contact shear, it also grasps the debris layer formation driving force. Fig 16. compares the evolution of this parameter along the contact surface to those of the debris layer and the maximum crack lengths, for both R3 and C10 contact configurations. A very satisfying correlation is observed. Thus, the Ruiz parameter Γ can reasonably predict the crack nucleation location within the fretted interface.

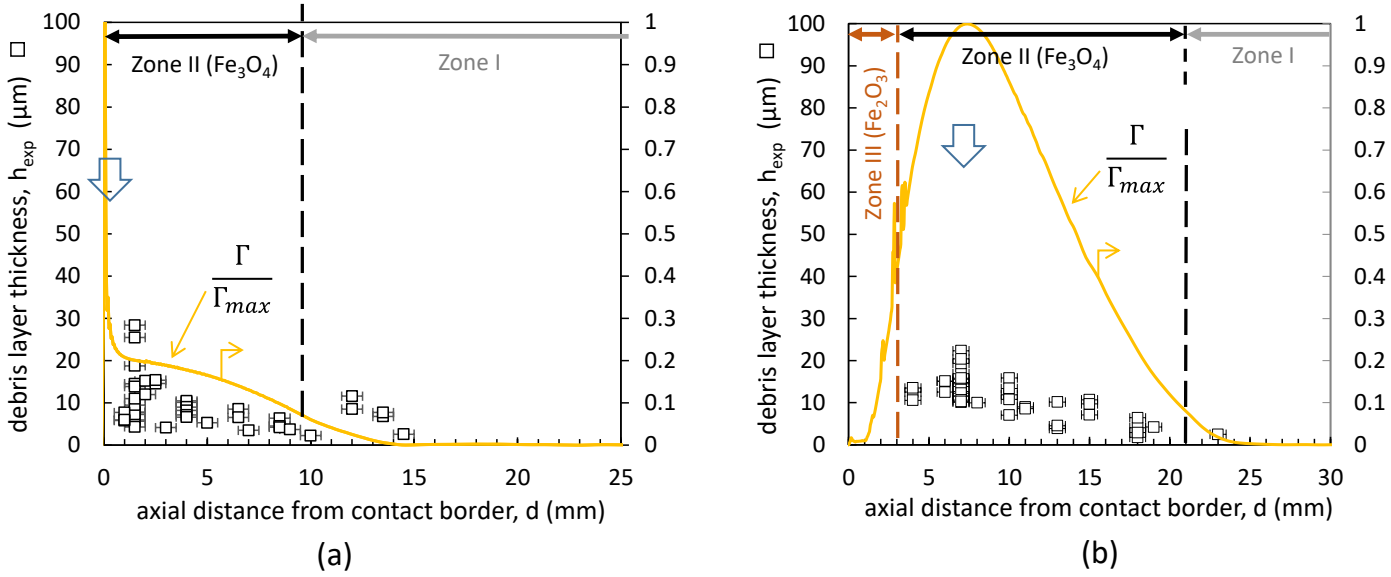

Fig. 17: Comparison between the debris layer thickness (h) and the $\boldsymbol{\Gamma}$ parameter for R3_12KN (a) and C10_15KN (b) contact configurations; Comparison between the crack length (a) and the $\boldsymbol{\Gamma}$ parameter for R3_12KN (a) and C10_15KN (b) contact configurations; (the blue arrow indicate the crack nucleation location predicted by the model).

5.2 Lifespan predictions

Stress computation without considering the debris layer

The Ruiz parameter Γ appears pertinent to predict the crack nucleation location but, it does not permit to predict the fretting-fatigue lives directly, as it cannot be compared straight away with the fatigue data of the material. Hence a sequential strategy is proposed. First the crack location is predicted by defining the position of the maximum value of the Γ parameter in the interface so called $X_{\Gamma max}$. Then, to predict the fretting-fatigue endurance, the SWT fatigue stress parameter is computed at this position, leading to the so called $\sigma_{SWT}(X_{\Gamma max})$ strategy.

A first analysis is done without including the presence of the debris layer. Figure 17 compares the life predictions for R3 and C10 fretting-fatigue specimens with Wöhler curve of the material for uniaxial fatigue. All the stress parameters have been normalized by the endurance limit in push-pull. The datapoints from the simulations are far below the Wöhler curve, suggesting and under estimation of the contact stresses operating within the fretted interface.

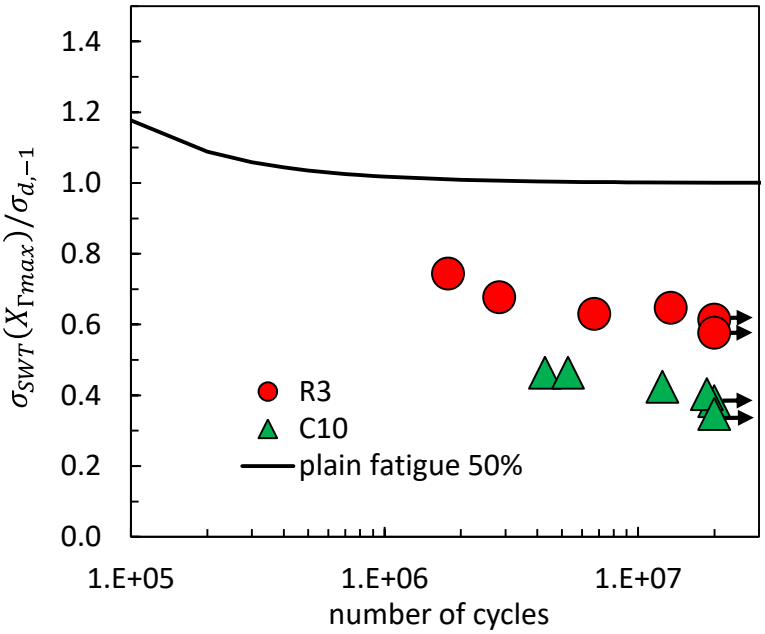

Fig. 18: Comparison between $\boldsymbol{\sigma_{SWT}(X_{\Gamma max})}$ and the fatigue property of the material (Without including the presence of the debris layer in the FEM modelling).

Stress computation with consideration of the debris layer

The model was modified to include a debris layer, as observed for the R3_12KN and C10_15KN contact configurations. The third body layer is modelled simply as a modification of the axle geometry, since it has been shown that the Young's modulus of a debris layer does not influence significantly the stress state [24], [25]. The shape of the third body layer was chosen as a simplified segmented boundary of the debris layer shown in Fig. 13 (dotted lines). The maximal height for each third body layer is set to h_{num} = 30 µm, based on the maximal layer thickness measured on specimens R3_12kN and C10_15kN, around 30 µm and 25 µm respectively.

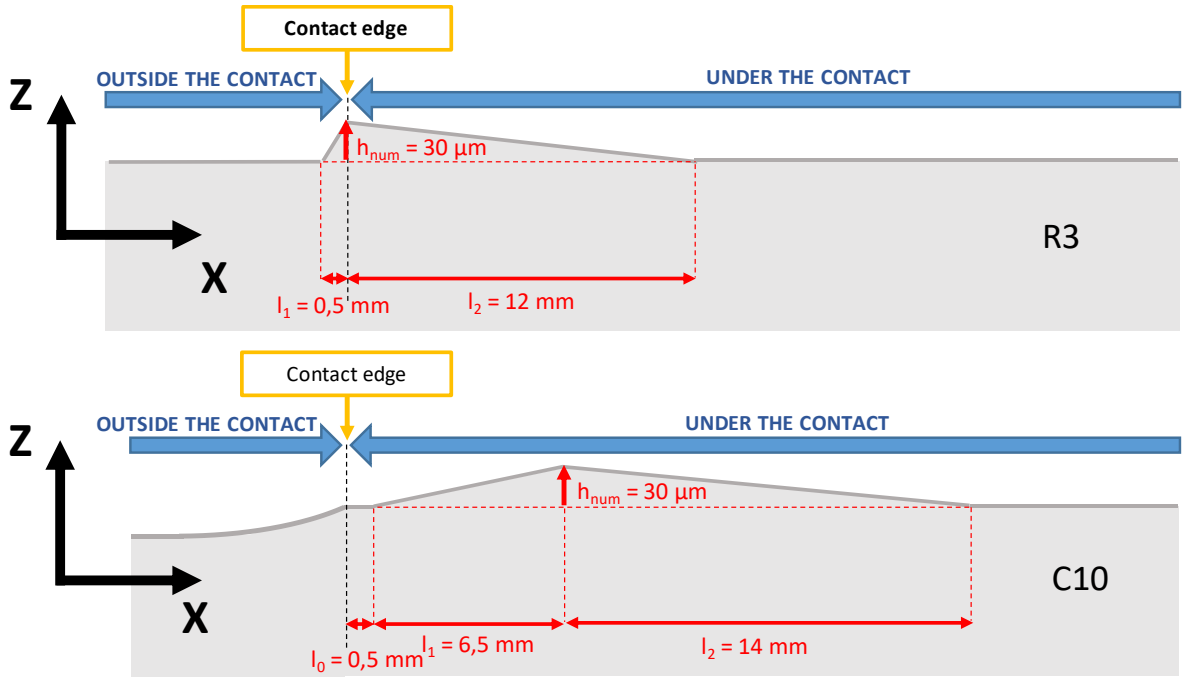

Fig. 19: Modelled third body layer shape for both sleeve border configuration.

The presence of the debris layer dramatically modifies the pressure profile along the interface, as shown by Fig. 20. It creates very high pressure peaks at the top of the modelled debris layer, resulting in high local stresses. These levels of pressure would likely induce plastic flow, which is consistent with the deformed shape of the surface debris. The shape of the modelled debris layer also induces opening of the contact (zones where the contact pressure is zero). This phenomenon seems exaggerated, and is the direct consequence of the strong hypothesis of the debris layer geometry. It is not however contradicted by experimental observation, as the modelling choice was to shape the debris layer in a stabilized state, neglecting the progressive build-up of this layer [25]. The debris and traces of contact seen in the zone predicted to be open could have been generated before the complete build-up of the layer, and thus before the local opening of the contact.

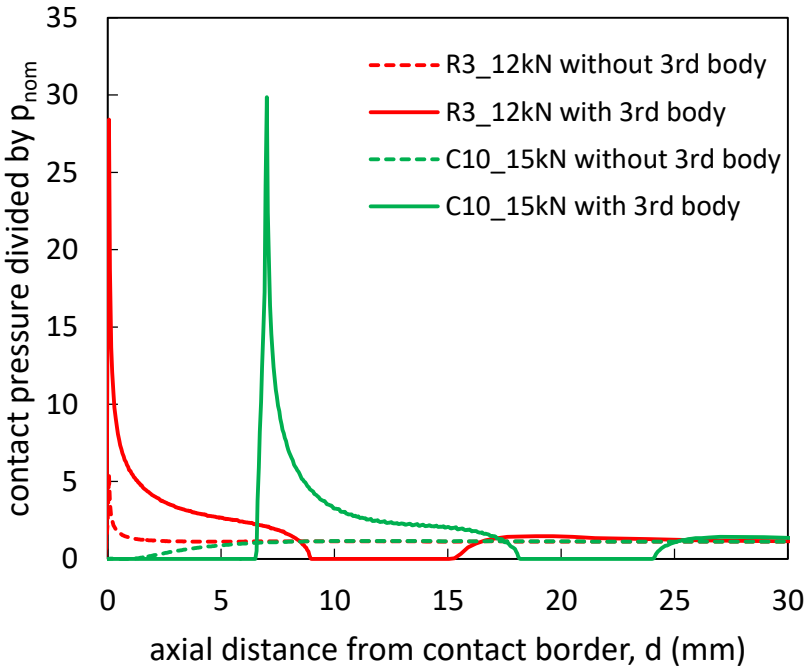

Fig. 20: Numerically calculated contact pressure profiles for R3_12kN and C10_15kN, without and with third body layer.

Then, considering this surface geometry modification, the $\sigma_{SWT}(X_{\Gamma max})$ strategy is applied. Fig. 21 compares the new predictions with the Wöhler curve of the material. Compared to the former analysis (i.e. without considering the debris layer, Fig. 18), a single master curve combining both R3 and C10 results and converging towards the fatigue limit of the material is now achieved. As detailed by Arnaud et al. [26], this definitely confirms the necessity to consider the debris layer entrapped within the fretted interface to properly predict the fretting fatigue endurance. However, the observed finite endurance values appear longer than the one predicted by the model. This might be due to the fact that the SWT fatigue stress analysis neglects the propagation phase. Indeed, at the fatigue limit, the endurance can be related to the crack nucleation condition and the propagation stage can be neglected. This condition is well captured by the given SWT fatigue stress analysis. However, under finite endurance condition, the total endurance also depends on the propagation stage. It can be significant under fretting fatigue conditions, particularly when, like in the present situation, the bulk fatigue stress is low (below 33 % of $\sigma_{d,-1}$). Besides, the dimension of the specimen may imply a long propagation extension before the specimen failure.

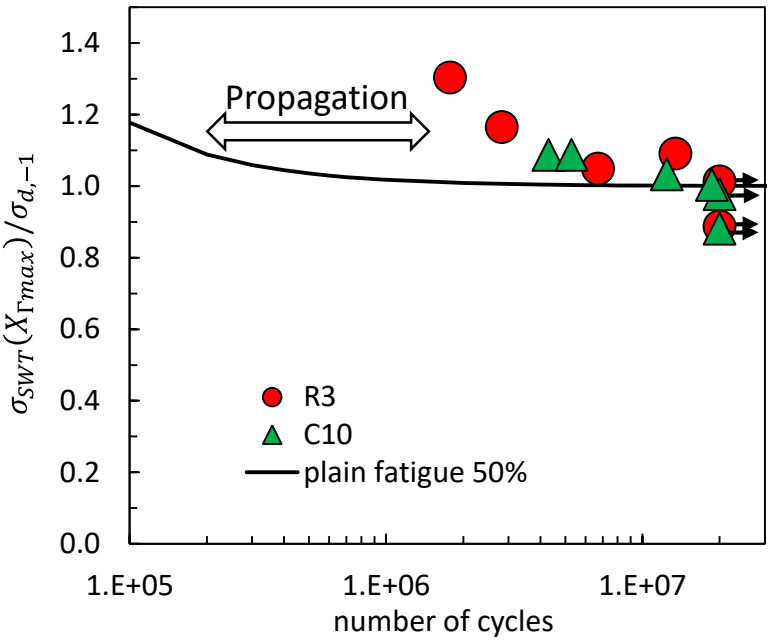

Fig. 21: Wohler curve SWT, and fatigue data for fully reversed tensile fatigue test.

This investigation also underlines the prime influence of the debris bed and related third maximum thickness *h* regarding the cracking risk. This is clearly illustrated in Figure 21 where the $\sigma_{SWT}(X_{\Gamma max})$ stress is plotted as a function of height the debris layer. It is interesting to see that a debris layer thickness of less than 30µm can increase by a factor 2.5 the $\sigma_{SWT}(X_{\Gamma max})$ stress for the C10 configuration and more than 1.6 for the R3 configuration. Hence this investigation outlines the crucial interest to consider the presence of the debris bed in the rotating bending shrink fitted assemblies to properly predict the fretting fatigue cracking risk.

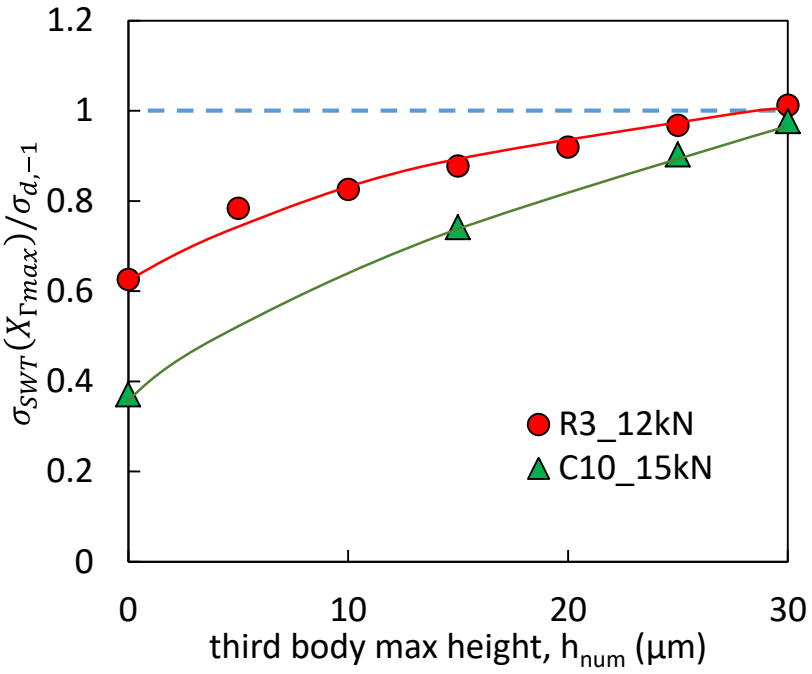

Fig. 22: Influence of the maximal third body layer on the maximal σ value for R3_12kN and C10_15kN specimens.

6 DISCUSSION REGARDING THIRD BODY DEBRIS LAYER

One hypothesis of the model is that the debris bed implemented with the FEM method is constant and does not evolve with additional loading cycles. Indeed, the debris formation implies material removal at the fretting interfaces. If the material removal is continuous, it should be expected a continuous increase of the debris layer thickness since the specific volume of oxide debris is significantly larger than the original metallic materials. To answer this question it is necessary to consider the theory of the third body developed by Fillot *et al*. [27]. As illustrated in Fig. 23, in the case of a tribological system allowing the debris ejection (Fig. 23a), the thickness of the bed of debris (third body) stabilizes when the debris formation flow equals the debris ejection flow leading to a constant third body debris layer thickness ($h_{tb,ss}$: steady state third body thickness) [27]. In our case, the debris ejection flow can be considered as negligible considering the dimension of the contact size. Thus, the thickness increases with the debris formation flow. However, the thicker the debris layer, the higher is the friction energy consumed within this layer. Consequently, a lower amount of friction energy is transmitted to the bulk material, decreasing its degradation and the new debris generation. Thus, the debris formation flow decreases continuously until it reaches a zero value when all the friction energy is consumed by the 3rd body layer (Fig. 23b). We can therefore assume that the observed interfaces well correspond to a steady state situation with

constant additional debris bed layers. An interesting remark deduced from this theory is that for a given material tribocouple, a system which is not allowing the debris ejection will systematically induce a thicker stabilized debris bed than observed for tribo system allowing the ejection. This conclusion is indirectly confirmed by the observed debris layer thicknesses exceeding 30 µm whereas in common small contact (sphere/plane), favoring the debris ejection, the latter does not exceed usually 10 to 15 µm.

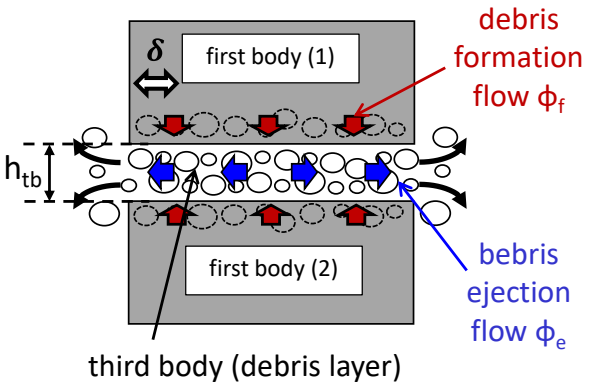

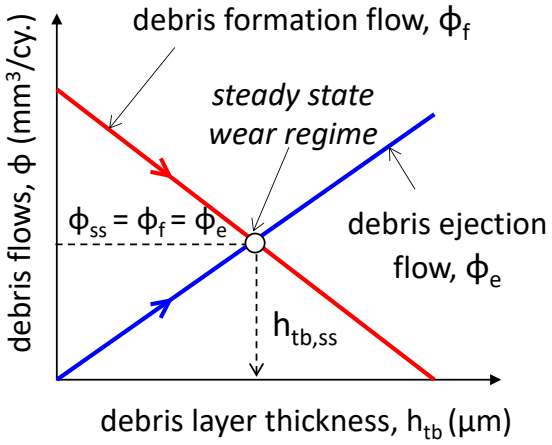

(a)

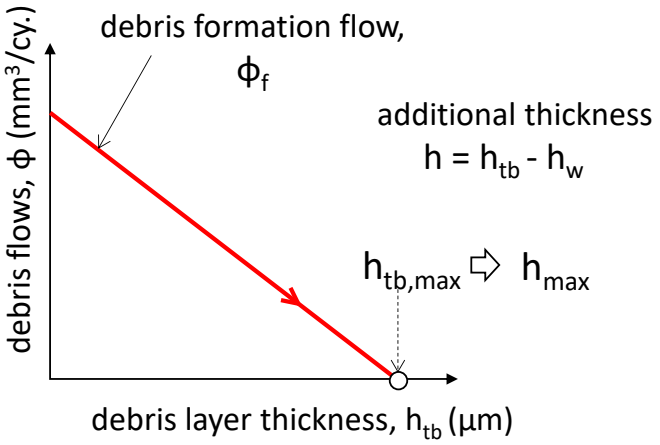

(b)

Fig. 23: (a) Illustration of the 3rd body theory for a tribological system allowing the debris ejection (determination of a stabilized thickness ($h_{tb,ss:}$ steady state third body thickness) via a balance between the debris flow ejection and the debris formation flow [25], [27]; (b) Illustration of the 3rd body theory in the present context where the ejection process is not effective: determination of a maximum stabilized thickness ($h_{tb,ss} = h_{tb,max}$) when all the friction energy is consumed but the debris layer and no additional wear debris can be formed.

However, one limitation of given model concerns the simplified segmented description of the debris bed shape involving sharp geometrical discontinuities which might overestimate the stress concentration. Hence, deeper investigations focusing on the debris shape effect need to be considered. Note that the continuous simulation of the debris bed formation in 2D contact configuration [25], [26], that we expect to transpose in this 3D simulation in a coming development, provides more continuous debris bed shapes which are certainly more representative of the contact reality. Future developments also need to better describe the rheological behaviour of the entrapped debris bed layer involving representative elastic-plastic constitutive laws. Even though Yue *et al.* [24] showed the limited influence of the third body's Young's modulus on stress states, these investigations were performed for regular and flat third body layers. In the case of sharp discontinuities, mechanical properties such as the Young's modulus would certainly influence stress concentration. Moreover, as the debris layer thickness has not been measured for all specimens, the use of one fixed shape and debris height for each geometry may be questioned. Available experimental data are too scarce too allow debris layer thickness prediction for now. Another aspect concerns the stress gradient effect. In most common fretting fatigue situations, the contact induces severe stress gradients which must be addressed applying for instance fatigue stress averaging procedures through a representative "process volume" [28], [29] or considering the critical distance method [30]. In the present situation, neglecting debris layer effects, the stress values inducing cracking are far below the fatigue limit (Fig. 18) and very low stress gradient are in fact imposed considering the very low nominal contact pressure (i.e. p_{nom} < 30 MPa). Hence, in a first approximation, the stress gradient effect can be neglected and hot spot stress analysis appears relevant. However, assuming the debris layer effect, stress discontinuities are occurring suggesting that again stress gradient effect should be considered. However, as mentioned previously, this will require a complete debris layer – stress gradient analysis which at this stage of our developments cannot be addressed.

Nevertheless, despite these various limitations, this given approach based on the $\sigma_{SWT}(X_{\Gamma max})$ strategy including in the FEM simulation the presence of a fretting wear debris layer entrapped within the interface, appears as reliable in order to predict the infinite endurance of rotating bending shrink fitted assemblies enduring fretting-fatigue. Assuming the third body theory, we suggest that the applied debris layer morphology can be considered as stable after limit number of loading cycles. However, a key aspect which is not addressed in the present work but currently motivating our future research work will consist in simulating the progressive formation of the

debris layer, in order to achieve a complete simulation of fretting fatigue cracking process involving crack nucleation but also crack propagation [31].

7 CONCLUSIONS

Rotating bending tests have been conducted on twelve shrink-fitted assemblies with a low contact pressure (less than 30 MPa), composed of a steel shaft and a bronze sleeve. Two sleeve border geometries have been compared. The following results were obtained:

- All specimen displayed fretting-fatigue damage, leading in some cases to large cracks or even complete breakage. The stuck, sliding and detachment zones, as well as the crack depths, angles and positions were documented.
- One of the geometries (C10) displays a better endurance.
- The investigation underlines that the Ruiz's criterion well predicts the location of the incipient crack nucleation as well as the maximum debris layer thickness. However the Ruiz's criterion (Γ) cannot permit the correlation with material fatigue data. Hence an original $\sigma_{SWT}(X_{\Gamma max})$ strategy is introduced: the location of the crack nucleation is estimated from the maximum value of Ruiz's criterion (Γ_{max}), then at this position, the fatigue endurance is estimated by computing the SWT fatigue stress.
- The $\sigma_{SWT}(X_{\Gamma max})$ approach applied without considering the presence of the debris layer provides failure predictions far below the Wöhler curve of the material. However, by simulating the presence of the debris layers, an endurance master curve combining both R2 and C10 results is achieved. The model also predicts an infinite endurance value consistent with the fatigue limit of the studied material. However for finite endurance conditions, the propagation stage needs to be considered.

ACKNOWLBORDERMENTS

The authors would like to thank The French Defense Procurement Agency (DGA) and the Defense Innovation Agency (AID) for the financial support of this work.

REFERENCES

[1] D. A. Hills, D. Nowell, et J. J. O'Connor, « On the mechanics of fretting fatigue », *Wear*, vol. 125, n° 1-2, p. 129-146, juill. 1988, doi: 10.1016/0043-1648(88)90198-6.

[2] K. Nakazawa, N. Maruyama, et T. Hanawa, « Effect of contact pressure on fretting fatigue of austenitic stainless steel », *Tribology International*, vol. 36, n° 2, p. 79-85, févr. 2003, doi: 10.1016/S0301-679X(02)00135-4.

[3] B. Alfredsson, « Fretting fatigue of a shrink-fit pin subjected to rotating bending: Experiments and simulations », *International Journal of Fatigue*, vol. 31, n° 10, p. 1559-1570, oct. 2009, doi: 10.1016/j.ijfatigue.2009.04.019.

[4] J. Wang et Y. Gao, « Numerical and experimental investigations on fretting fatigue properties of GH4169 superalloy at the elevated temperature », *International Journal of Fatigue*, vol. 149, p. 106274, août 2021, doi: 10.1016/j.ijfatigue.2021.106274.

[5] C. Song, M. X. Shen, X. F. Lin, D. W. Liu, et M. H. Zhu, « An investigation on rotatory bending fretting fatigue damage of railway axles », *Fatigue & Fracture of Engineering Materials & Structures*, vol. 37, n° 1, p. 72-84, janv. 2014, doi: 10.1111/ffe.12085.

[6] A. Yameogo, « Étude expérimentale et numérique de l'amorçage et de la propagation de fissures de fretting dans un assemblage roue/essieu ferroviaire », École Centrale Paris, 2004.

[7] D. H. Lee, B. C. Goo, C. W. Lee, J. B. Choi, et Y. J. Kim, « Fatigue Life Evaluation of Press-Fitted Specimens by Using Multiaxial Fatigue Theory at Contact Edge », *Key Engineering Materials*, vol. 297-300, p. 108-114, nov. 2005, doi: 10.4028/www.scientific.net/KEM.297-300.108.

[8] E. Leidich, B. Brůžek, et J. Vidner, « Investigation on the Shrink-fitted Assemblies with a Circumferential Groove », p. 8, 2016.

[9] T. Rauert, J. Herrmann, P. Dalhoff, et M. Sander, « Fretting fatigue induced surface cracks under shrink fitted main bearings in wind turbine rotor shafts », *Procedia Structural Integrity*, vol. 2, p. 3601-3609, 2016, doi: 10.1016/j.prostr.2016.06.449.

[10] Y. Zhang, L. Lu, Y. Gong, J. Zhang, et D. Zeng, « Fretting wear-induced evolution of surface damage in press-fitted shaft », *Wear*, vol. 384-385, p. 131-141, août 2017, doi: 10.1016/j.wear.2017.05.014.

[11] L. Bertini et C. Santus, « Fretting fatigue tests on shrink-fit specimens and investigations into the strength enhancement induced by deep rolling », *International Journal of Fatigue*, vol. 81, p. 179-190, déc. 2015, doi: 10.1016/j.ijfatigue.2015.08.007.

[12] S. Kowalski, « Assessment of the condition of the finish-rolled shaft top layer for fretting wear development », *Wear of materials*, 2021.

[13] L. Petureau, V. Doquet, et B. Dieu, « Influence of a static torque on plasticity and asperity-induced closure effects during fatigue crack growth in bainitic steel cylinders loaded in push-pull »,

International Journal of Fatigue, vol. 155, p. 106628, févr. 2022, doi: 10.1016/j.ijfatigue.2021.106628.

[14] K. Nishioka et H. Komatsu, « Researches on Increasing the Fatigue Strength of Press-Fitted Shaft Assembly », *Bulletin of JSME*, vol. 10, n° 42, p. 880-889, 1967, doi: 10.1299/jsme1958.10.880.

[15] A. Leluan, « Assemblages frettés ». Techniques de l'Ingénieur, 1986.

[16] M. Lorenzo, J. C. Pérez-Cerdán, et C. Blanco, « Influence of the Thermal Assembly Process on the Stress Distributions in Shrink Fit Joints », *KEM*, vol. 572, p. 205-208, sept. 2013, doi: 10.4028/www.scientific.net/KEM.572.205.

[17] S. Baydoun, S. Fouvry, S. Descartes, et P. Arnaud, « Fretting wear rate evolution of a flat-on-flat low alloyed steel contact: A weighted friction energy formulation », *Wear*, vol. 426-427, p. 676-693, avr. 2019, doi: 10.1016/j.wear.2018.12.022.

[18] Y. Shu, G. Yang, et Z. Liu, « Experimental study on fretting damage in the interference fit area of high-speed train wheels and axles based on specimen », *Engineering Failure Analysis*, vol. 141, p. 106619, nov. 2022, doi: 10.1016/j.engfailanal.2022.106619.

[19] D. H. Lee, S. J. Kwon, J. B. Choi, et Y. J. Kim, « Observations of Fatigue Damage in the Press-Fitted Shaft under Bending Loads », *Key Engineering Materials*, vol. 326-328, p. 1071-1074, déc. 2006, doi: 10.4028/www.scientific.net/KEM.326-328.1071.

[20] J. M. Bailey et D. Godfrey, « Coefficient of friction and damage to contact area during the early stages of fretting, II - Steel, Iron, Iron Oxyde, and Glass combinations ». NACA TN 3144, 1954.

[21] E. Radi, L. Lanzoni, A. Strozzi, et E. Bertocchi, « Shaft-hub press fit subjected to bending couples: Analytical evaluation of the shaft-hub detachment couple », *Applied Mathematical Modelling*, vol. 50, p. 135-160, oct. 2017, doi: 10.1016/j.apm.2017.05.018.

[22] K. N. Smith, P. Watson, et T. H. Topper, « A Stress-Strain Function for the Fatigue of Metals », *Journal of Materials*, vol. 5, n° 4, p. 767-778, 1970.

[23] C. Ruiz, P. H. B. Boddington, et K. C. Chen, « An investigation of fatigue and fretting in a dovetail joint », *Experimental Mechanics*, vol. 24, n° 3, p. 208-217, sept. 1984, doi: 10.1007/BF02323167.

[24] T. Yue et M. Abdel Wahab, « A Numerical Study on the Effect of Debris Layer on Fretting Wear », *Materials*, vol. 9, n° 7, p. 597, juill. 2016, doi: 10.3390/ma9070597.

[25] P. Arnaud et S. Fouvry, « A dynamical FEA fretting wear modeling taking into account the evolution of debris layer », *Wear*, vol. 412-413, p. 92-108, oct. 2018, doi: 10.1016/j.wear.2018.07.018.

[26] P. Arnaud et S. Fouvry, « Modeling the fretting fatigue endurance from partial to gross slip: The effect of debris layer », *Tribology International*, vol. 143, p. 106069, mars 2020, doi: 10.1016/j.triboint.2019.106069.

[27] N. Fillot, I. Iordanoff, et Y. Berthier, « Wear modeling and the third body concept », *Wear*, vol. 262, n° 7-8, p. 949-957, mars 2007, doi: 10.1016/j.wear.2006.10.011.

[28] S. Fouvry, P. Kapsa, et L. Vincent, « A multiaxial fatigue analysis of fretting contact taking into account the size effect », *ASTM STP 1367*, p. 167-182, 2000.

[29] H. Proudhon, S. Fouvry, et J. Buffiere, « A fretting crack initiation prediction taking into account the surface roughness and the crack nucleation process volume », *International Journal of Fatigue*, vol. 27, n° 5, p. 569-579, mai 2005, doi: 10.1016/j.ijfatigue.2004.09.001.

[30] J. Araújo et D. Nowell, « The effect of rapidly varying contact stress fields on fretting fatigue », *International Journal of Fatigue*, vol. 24, n° 7, p. 763-775, juill. 2002, doi: 10.1016/S0142-1123(01)00191-8.

[31] D. Erena, J. Vázquez, C. Navarro, et R. Talemi, « Numerical study on the influence of artificial internal stress relief groove on fretting fatigue in a shrink-fitted assembly », *Tribology International*, vol. 151, p. 106443, nov. 2020, doi: 10.1016/j.triboint.2020.106443.